

# Antiferromagnetic diamond network as an efficient spin filter: Proposition of a spin-specific semi-conducting behavior

Debjani Das Gupta<sup>1,\*</sup> and Santanu K. Maiti<sup>1,†</sup>

<sup>1</sup>*Physics and Applied Mathematics Unit, Indian Statistical Institute,  
203 Barrackpore Trunk Road, Kolkata-700 108, India*

(Dated: February 18, 2025)

We propose, for the first time, that an array of diamond plaquettes, each possessing vanishing net magnetization, can achieve complete spin polarization over a broad bias window. Furthermore, this system can be utilized to realize spin-specific semiconducting behavior. We describe the antiferromagnetic diamond network within a tight-binding framework, where spin-dependent scattering arises due to the interaction between itinerant electrons and local magnetic moments at different lattice sites. The mechanism underlying spin filtration relies on the specific arrangement of magnetic moments within individual plaquettes. We systematically investigate the spin polarization phenomenon under various input conditions, examining its dependence on network size, system temperature, and the magnetic flux threading each plaquette. Due to the network's geometry, we identify a sharply localized, highly degenerate energy level coexisting with conducting states. By tuning physical parameters, a small energy gap can be established between these degenerate localized states and the conducting energy band, enabling spin-specific *p*-type and *n*-type semiconducting behavior. Our findings offer a novel approach for designing future spintronic devices based on similar antiferromagnetic networks.

## I. INTRODUCTION

Antiferromagnetic (AFM) systems are emerging as promising candidates for next-generation spintronic technology<sup>1-8</sup>. Over a decade ago, when researchers first incorporated electron spin alongside charge in micro-electronic devices, ferromagnetic (FM) materials were the preferred choice<sup>9-14</sup>. Ferromagnetic materials facilitate global spin polarization due to their long-range magnetic ordering. However, as technology advances, there is a growing demand for enhanced functionality, reduced power consumption, and miniaturized device architectures. In this context, AFM spintronic elements present several advantages over conventional FM materials. AFM systems can function as multilevel switches<sup>15,16</sup> and, crucially, do not generate stray fringe fields, ensuring that their performance remains unaffected by external magnetic perturbations<sup>17</sup>. Moreover, they enable electronic writing pulse frequencies in the terahertz regime<sup>5,18</sup> and exhibit higher ordering temperatures compared to FM materials, allowing operation near room temperature<sup>3,4</sup>. Given these advantageous properties, AFM materials have been established as efficient components in spintronic applications<sup>4-6</sup>.

In spin-based electronic devices, a fundamental objective is to spatially separate spin-up and spin-down electrons along their transport path, enabling the utilization of spin degrees of freedom alongside charge transport. Achieving this requires the presence of spin-dependent scattering within the system. When an electron moves at a sufficiently high velocity, the interaction between its angular momentum and spin effectively generates a magnetic field in its rest frame. This phenomenon, known as spin-orbit interaction (SOI), produces an effective magnetic field that facilitates the separation of spin channels<sup>19,20</sup>. In solid-state systems, two primary types of SOI are typically considered: Rashba and Dresselhaus interactions. The Rashba interaction arises due

to structural inversion asymmetry in the confining potential<sup>21</sup>, while the Dresselhaus interaction originates from bulk inversion asymmetry<sup>22</sup>. Although SOI-based spin-dependent scattering mechanisms offer several advantages, a significant limitation is the generally weak spin-orbit coupling strength in most materials<sup>23</sup>. This weak interaction reduces the efficiency of spin channel separation, making it challenging to achieve high spin currents and effective spin filtration over a reasonable bias window.

Given the inherent limitations of spin-orbit-coupled and ferromagnetic materials, recent breakthrough studies on antiferromagnetic (AFM) systems suggest that these materials offer a more suitable and reliable platform for the future development of spintronic devices with advanced functionalities. In general, the transmission spectra for spin-up and spin-down electrons are identical in AFM materials, resulting in no net spin current unless specific symmetry-breaking conditions are introduced. One approach to achieving spin polarization in AFM systems is to introduce asymmetric hopping in selective regions, thereby creating distinct transport environments for spin-up and spin-down electrons. Alternatively, a disparity in onsite potential can enable electrons of different spins to propagate through separate energy channels<sup>24</sup>. Various methods have been proposed to induce asymmetric hopping in different geometric configurations. Additionally, chirality combined with an external electric field can create spin-dependent potential energy variations in AFM molecular systems<sup>25,26</sup>. The efficiency of spin filtration is enhanced in AFM helical structures with long-range hopping order. However, in the absence of helicity or an applied electric field, spin separation is completely suppressed.

We seek a system where spin channel separation can be achieved without the application of an external electric field, even in the presence of symmetric hopping. In this work, we demonstrate that a mesoscopic chain with a spe-

cific geometric structure—comprising multiple loops and exhibiting zero net magnetization—can generate fully spin-polarized current (see Fig. 1). The proposed antiferromagnetic network consists of multiple diamond plaquettes, each containing four magnetic sites arranged such that the net magnetization of each plaquette remains zero. The motivation for considering this geometry is multifaceted. First, looped structures inherently exhibit nontrivial quantum interference effects due to the presence of multiple electronic transport paths<sup>27–31</sup>, distinguishing them from conventional loopless systems. Second, by ensuring that each diamond plaquette has zero net magnetization, the symmetry between spin-up and spin-down Hamiltonians is naturally broken, enabling spin-selective electron transmission through the network. Third, this specific geometry gives rise to a sharply localized energy level coexisting with conducting energy states. Notably, this localized level is highly degenerate, facilitating spin-specific semiconducting behavior. These findings suggest a new design paradigm for efficient electronic and spintronic devices, where spin channel separation can be realized without explicit symmetry breaking or external field application. Instead, multiple AFM loop substructures inherently enable spin-selective transport, paving the way for novel spintronic architectures.

We simulate the antiferromagnetic diamond network within a tight-binding (TB) framework. The presence of a sharply localized energy level is analytically determined from the energy dispersion relation of the network. To investigate spin-selective electron transport, we couple a finite-sized diamond network to two contact electrodes and compute the two-terminal transmission probabilities using the Green’s function formalism. The spin-dependent currents are then evaluated using the Landauer-Büttiker formula, allowing us to determine the spin polarization coefficient. To explore the tunability of spin filtration efficiency, we introduce a finite magnetic flux through each plaquette and observe that the phase of spin polarization can be selectively modified. Notably, the sharply localized energy level vanishes when a magnetic flux  $\phi$  is applied but re-emerges at half the flux quantum ( $\phi/2$ ). The spin-selective semiconducting behavior is directly linked to this degenerate localized energy level. By appropriately adjusting the Fermi energy, the system can exhibit either p-type or n-type spin-dependent semiconducting properties. Furthermore, we critically analyze the effects of system temperature and size to ensure a comprehensive understanding of the proposed model.

The remainder of this paper is organized as follows. Section II describes the junction setup, tight-binding Hamiltonian, and theoretical framework for the calculations. Section III presents the main results and is divided into three subsections. First, we analytically derive the energy band structure and examine the behavior of the localized states in the presence of a magnetic flux. Next, we discuss possible tuning mechanisms for spin polarization. Finally, the last subsection explores spin-dependent semiconducting behavior. A summary of our findings is provided in Sec. IV.

## II. MODEL AND THEORETICAL FORMALISM

### A. Model Description and Tight-Binding Hamiltonian

We consider a system composed of an array of square lattice units connected diagonally by a single bond. This array is coupled to two non-magnetic leads at its extremities: a source (S), where electrons are injected, and a drain (D), where electrons are collected. The schematic representation of the system is shown in Fig. 1.

Within the diamond-like plaquette structure, two distinct atomic positions exist. At sites 1 and 3 (see Fig. 1), atoms have two nearest neighbors, these are labeled as

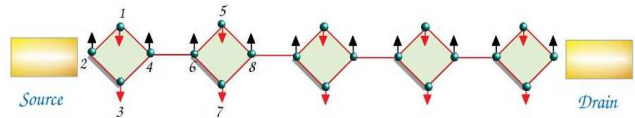


FIG. 1: (Color online). Schematic of the junction setup, where an antiferromagnetic diamond network is coupled to source and drain electrodes.

A-type atoms. In contrast, sites 2 and 4 host atoms with three nearest neighbors, referred to as B-type atoms. The local magnetic moments are aligned along the  $-Z$  direction at A-type sites and along the  $+Z$  direction at B-type sites.

To describe the system, we employ a tight-binding (TB) Hamiltonian considering only nearest-neighbor hopping in the non-interacting case. Each magnetic site  $i$  contains a net spin  $\langle \vec{s}_i \rangle$ . When an itinerant electron interacts with this site, spin-dependent scattering occurs, described by<sup>23,32,33</sup>  $J\langle \vec{s}_i \rangle \cdot \vec{\sigma} = \vec{h}_i \cdot \vec{\sigma}$ , where  $J$  represents interaction strength, and  $\vec{\sigma}$  denotes the Pauli matrices in the  $\sigma_z$  diagonal basis. We refer to  $\vec{h}_i (= J\langle \vec{s}_i \rangle \cdot \vec{\sigma})$  as the spin-dependent scattering factor. This interaction modifies the site potential as:  $\epsilon_i \rightarrow \epsilon_i - \vec{h}_i \cdot \vec{\sigma}$ .

The tight-binding Hamiltonian governing the system is expressed as:

$$\mathcal{H} = \sum_i \left[ c_i^\dagger \left( \epsilon_i - \vec{h}_i \cdot \vec{\sigma} \right) c_i + c_{i+1}^\dagger t_i c_i + h.c. \right], \quad (1)$$

where  $c_i^\dagger = \begin{pmatrix} c_{i\uparrow}^\dagger & c_{i\downarrow}^\dagger \end{pmatrix}$ , with  $c_{i\sigma}^\dagger$  and  $c_{i\sigma}$  being the creation and annihilation operators at site  $i$  for spin  $\sigma = (\uparrow, \downarrow)$ , respectively. The net spin  $\langle \vec{s}_i \rangle$  at site  $i$  is characterized by a polar angle  $\theta_i$  and an azimuthal angle  $\varphi_i$  in spherical coordinates.

The modified on-site potential is given by:

$$\epsilon_i - \vec{h}_i \cdot \vec{\sigma} = \begin{pmatrix} \epsilon_i - h \cos \theta_i & -h \sin \theta_i e^{-j\varphi_i} \\ -h \sin \theta_i e^{j\varphi_i} & \epsilon_i + h \cos \theta_i \end{pmatrix}. \quad (2)$$

Here, the spin-flip parameter magnitude  $h$  and the non-magnetic potential energy  $\epsilon_i$  are assumed to be identical for both spin-up and spin-down electrons at any given site.

The hopping energy matrix is given by:

$$\mathbf{t}_i = \text{diag}(t_i, t_i), \quad (3)$$

where  $t_i = t$  within a plaquette and  $t_i = t'$  between adjacent plaquettes.

### B. NEGF Method and Spin Polarization

We perform numerical calculations using the non-equilibrium Green's function (NEGF) method<sup>34</sup>. The average density of states (ADOS) is obtained by taking the imaginary part of the trace of the retarded Green's function:

$$\rho = - \left( \frac{1}{\pi N_s} \right) \text{Im}[\text{Tr}[\mathcal{G}^r]], \quad (4)$$

where  $N_s$  is the total number of sites in the system. The total number of diamond plaquettes is denoted by the parameter  $N$  ( $N_s = 4N$ ).

The transmission probability is given by:

$$T_{\sigma\sigma'} = \text{Tr}[\mathbf{\Gamma}_{S\sigma} \mathcal{G}^r \mathbf{\Gamma}_{D\sigma'} \mathcal{G}^a]. \quad (5)$$

where  $\mathcal{G}^r$  and  $\mathcal{G}^a$  are the retarded and advanced Green's functions respectively, and  $\mathbf{\Gamma}_{S\sigma}$  and  $\mathbf{\Gamma}_{D\sigma'}$  are the coupling matrices.

The retarded Green's function  $\mathcal{G}^r$  ( $\mathcal{G}^a = (\mathcal{G}^r)^\dagger$ ) is expressed as:

$$\mathcal{G}^r = (E - \mathcal{H} - \Sigma_S - \Sigma_D)^{-1}, \quad (6)$$

where  $\Sigma_S$  and  $\Sigma_D$  are the self-energies of the source and drain leads, respectively. The coupling matrices are related to the self-energies as  $\mathbf{\Gamma}_{S(D)} = -2\text{Im}[\Sigma_{S(D)}]$ .

We calculate the spin-resolved current using the Landauer-Büttiker formalism<sup>33,34</sup>. The total transmission probability  $T_\sigma$ , summed over the incident spin of the electron, is integrated over the full allowed energy window to obtain the current at a finite temperature  $\mathcal{T}$ . Under an applied voltage bias  $V$  between the two leads, the spin-dependent current is given by:

$$I_\sigma = \left( \frac{e}{h} \right) \int T_\sigma (f_S - f_D) dE. \quad (7)$$

Here,  $f_{S(D)}$  represents the Fermi function of the source (drain), expressed as:

$$f_{S(D)} = \left[ 1 + \exp \left( \frac{E - \mu_{S(D)}}{k_B \mathcal{T}} \right) \right]^{-1}, \quad (8)$$

where the electrochemical potentials of the leads are related to the Fermi energy  $E_F$  of the system as  $\mu_{S(D)} = E_F \pm eV/2$ .

The spin polarization is defined as the ratio of spin current to charge current:

$$P = \frac{I_\uparrow - I_\downarrow}{I_\uparrow + I_\downarrow}. \quad (9)$$

A value of  $P = \pm 1$  indicates complete spin polarization, while  $P = 0$  corresponds to equal spin-up and spin-down currents, resulting in zero net spin current and polarization.

## III. RESULTS AND DISCUSSION

### A. Spectral Analysis and Localization Behavior

We first examine the band structure of a diamond chain connected by a single bond. As shown in Fig. 2, we consider an infinite array of diamond plaquettes that are not connected to any reservoirs. We begin with the spinless case, where all sites are nonmagnetic. In the subsequent section, we extend these results to spin-dependent scattering, incorporating our actual antiferromagnetic (AF) model.

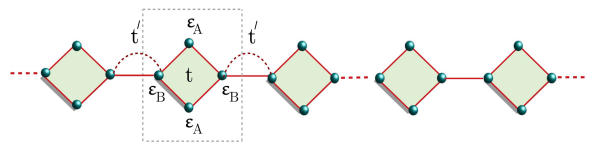


FIG. 2: (Color online). Infinite array of diamond plaquettes. We consider the spinless case, where two types of hopping energies are present:  $t$  within a plaquette and  $t'$  between adjacent plaquettes. The unit cell is indicated in the figure.

From the energy dispersion relation, we can identify the localization and conduction bands, which later help in determining the energy window for either spin-up or spin-

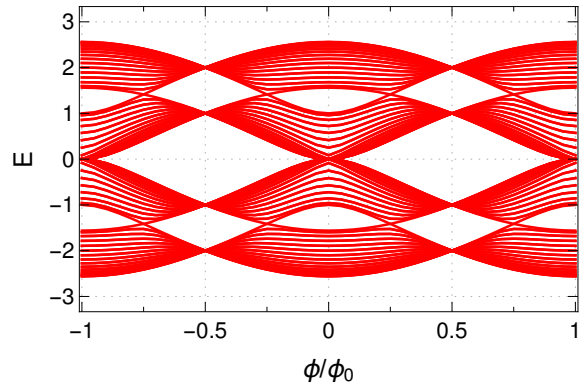


FIG. 3: (Color online). Variation of energy eigenvalues with magnetic flux. Four energy bands are observed, with band gaps appearing at specific values of  $\phi$ . We consider  $N = 20$  plaquettes under periodic boundary conditions to approximate an infinite diamond chain. The parameters used are  $\epsilon_A = \epsilon_B = 0$  and  $t = t' = 1$ .

down electrons. Each unit cell consists of four atomic sites, as shown in Fig. 2. There are two types of sites, labeled A and B, with intracell hopping energy  $t$  and intercell hopping energy  $t'$ . The effective onsite matrix and hopping matrix for a unit cell are given by

$$\epsilon_{\text{eff}} = \begin{pmatrix} \epsilon_A & t & 0 & t \\ t & \epsilon_B & t & 0 \\ 0 & t & \epsilon_A & t \\ t & 0 & t & \epsilon_B \end{pmatrix}, \quad \mathbf{t}_{\text{eff}} = \begin{pmatrix} 0 & 0 & 0 & 0 \\ 0 & 0 & 0 & 0 \\ 0 & 0 & 0 & 0 \\ 0 & t' & 0 & 0 \end{pmatrix}. \quad (10)$$

Furthermore, we can generalize this system to the presence of a magnetic flux. If a uniform magnetic field  $\vec{B}$  is applied along the  $Z$ -axis, threading a flux  $\phi$  through each

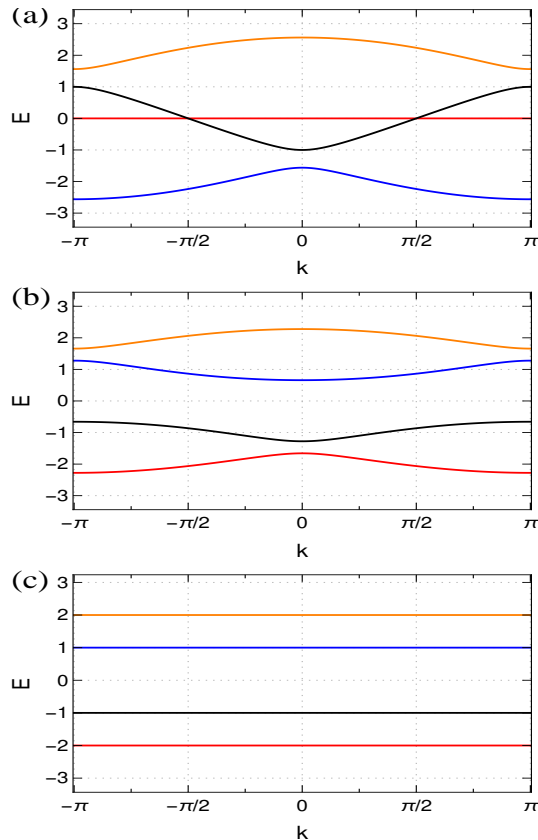


FIG. 4: (Color online).  $E - k$  relation for different magnetic flux values: (a)  $\phi = 0$ , (b)  $\phi = 0.35\phi_0$ , and (c)  $\phi = 0.5\phi_0$ . Different colors represent different energy bands. The parameters used are identical to those in Fig. 3.

loop, it induces a phase difference as electrons hop between sites within a diamond plaquette<sup>31,35</sup>. This modifies the hopping energy  $t$ , leading to a transformation:

$$t \rightarrow te^{j\eta}, \quad \text{where } \eta = \frac{\pi\phi}{2\phi_0}.$$

Here,  $\phi$  is measured in units of the flux quantum  $\phi_0 = hc/e$ .

To determine the energy dispersion relation, we solve the determinant equation:

$$\left| E\mathbf{I} - \epsilon_{\text{eff}} - e^{jk}\mathbf{t}_{\text{eff}} - e^{-jk}\mathbf{t}_{\text{eff}}^\dagger \right| = 0. \quad (11)$$

Several interesting features arise in the energy bands as the flux  $\phi$  varies. These effects are discussed in detail below.

By solving the above equation, we obtain the  $E - k$  relation for the spinless case in the presence of magnetic flux:

$$(E - \epsilon_A)^2 \left[ (E - \epsilon_B)^2 - t^2 \right] - 4t^2 (E - \epsilon_A) \left[ (E - \epsilon_B) + t' \cos 2\eta \cos k \right] + 2t^4 (1 - \cos 4\eta) = 0. \quad (12)$$

These energy eigenvalues (analytical expressions for various  $E - k$  relations are provided in the Appendix A for clarity) exhibit a periodicity of  $\phi_0$ , as illustrated in Fig. 3. Four energy bands are observed, with some bands touching at  $\phi/\phi_0 = 0$  or 1. The band gap maximizes at

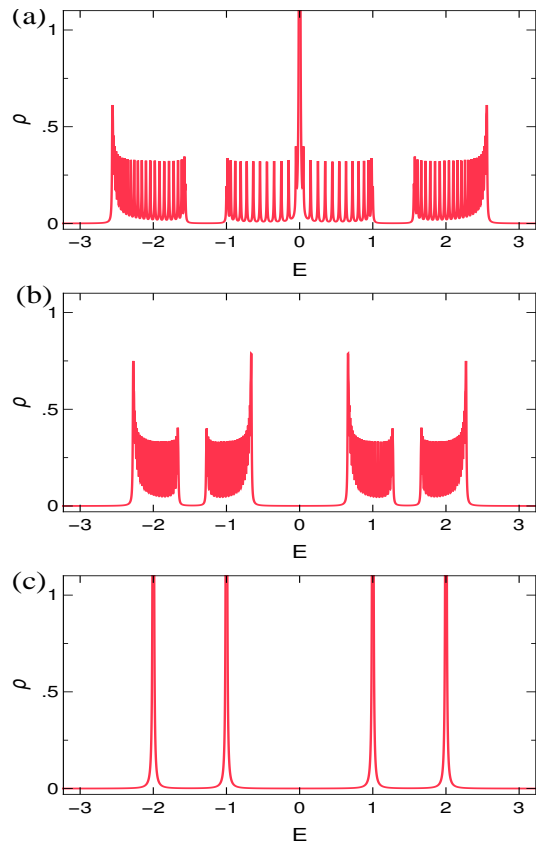


FIG. 5: (Color online). Average density of states for the same flux values as in Fig. 4. We consider  $N = 50$  plaquettes, with parameters identical to those in Fig. 3.

$\phi/\phi_0 = 0.5$ . To analyze localization behavior, we consider three distinct cases:

- **Case 1:**  $\phi = 0$  (no magnetic flux)

In the absence of a magnetic flux, the phase factor vanishes, simplifying Eq. 12. In this case, there always exists a solution  $E = \epsilon_A$ , independent of  $k$ , corresponding to a localized state (see Eq. A2a). This is depicted in Fig. 4(a), where a straight (red) line at  $E = 0$  indicates localization. The same is reflected in Fig. 5(a), where a sharp peak appears in the density of states.

- **Case 2:**  $0 < \phi < \phi_0/2$  (intermediate magnetic flux)

At intermediate values of  $\phi$ , all energy eigenvalues depend on  $k$ , eliminating localized states (see Eqs. A1a and A1b). Figure 4(b) shows the dispersion relation for  $\phi = 0.35\phi_0$ , where no localized states appear. The corresponding density of states in Fig. 5(b) further confirms their absence.

- **Case 3:**  $\phi = \phi_0/2$  (half flux-quantum)

At  $\phi = \phi_0/2$ , localized bands reappear. Unlike the zero-flux case, four distinct localized levels emerge at  $E = -2, -1, 1, \text{ and } 2$ , as observed in Fig. 4(c), following Eqs. A3a and A3b. The degeneracy of these states matches the number of diamond plaquettes,  $N$ , under periodic boundary conditions. The same is reflected in Fig. 5(c).

Now we analyze the spin-dependent energy band structure of our chosen antiferromagnetic system. Understanding the spin-dependent energy bands is crucial for realizing efficient spintronic devices. In our model, the magnetic moments are oriented along either the  $+Z$  or  $-Z$  axis, i.e.,  $\theta_i = 0$  or  $\pi$ , with  $\varphi_i = 0$ . This results in diagonal onsite and hopping energy matrices, allowing us

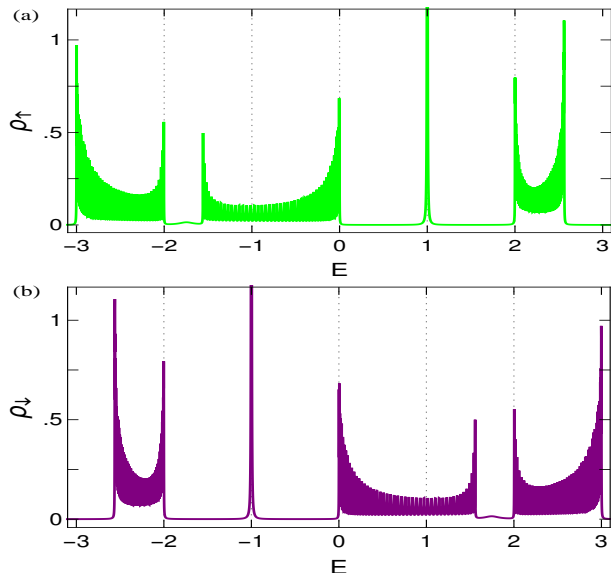


FIG. 6: (Color online). ADOS for (a) up spin and (b) for down spin in an AF diamond network with  $N = 50$ . The sharp peak at  $E = 1$  in (a) corresponds to a localized state for up spin, while in (b), the localized state for down spin is at  $E = -1$ . A finite energy gap between the conducting band and the localized state can lead to a spin-selective transport.

to decompose the Hamiltonian into two independent spin sub-spaces. In the AF network (Fig. 1), sites A (1,3,5,7) have magnetic moments  $\vec{h}(h, \pi, 0)$  along  $-Z$ , while sites B (2,4,6,8) have  $\vec{h}(h, 0, 0)$  along  $+Z$ . The spin-dependent onsite potentials are:

$$\epsilon_{A\uparrow} = \epsilon + h, \quad \epsilon_{B\uparrow} = \epsilon - h, \quad (13)$$

$$\epsilon_{A\downarrow} = \epsilon - h, \quad \epsilon_{B\downarrow} = \epsilon + h. \quad (14)$$

The dispersion relations are:

$$(E - \epsilon - h) \left[ (E - \epsilon + h) \left\{ (E - \epsilon)^2 - h^2 - 4t^2 \right\} - 4t^2 t' \cos k \right] = 0, \quad (15)$$

for up spin electrons, and

$$(E - \epsilon + h) \left[ (E - \epsilon - h) \left\{ (E - \epsilon)^2 - h^2 - 4t^2 \right\} - 4t^2 t' \cos k \right] = 0, \quad (16)$$

for down spin electrons. Equation 15 shows that up spin electrons form a localized level at  $E_{\uparrow} = \epsilon + h$ , while Eq. 16 indicates that down spin electrons localize at  $E_{\downarrow} = \epsilon - h$ . If a finite gap exists between the conducting and localized states, the Fermi energy can be tuned to enable transport of only one spin species, achieving spin filtering.

To have a clear understanding of different sub-bands, we compute ADOS for a finite AF network. For each spin case, the ADOS is determined by the relation

$$\rho_{\sigma} = -\frac{1}{\pi N_s} \text{Im}[\text{Tr}[\mathcal{G}_{\sigma}^r]], \quad (17)$$

where the retarded Green's function is defined as

$$\mathcal{G}_{\sigma}^r = (E - \mathcal{H}_{\sigma} - \Sigma_{S\sigma} - \Sigma_{D\sigma})^{-1}. \quad (18)$$

Using parameters  $\epsilon = 0$ ,  $t = t' = 1$ ,  $h = 1$ , and lead couplings  $\tau_S = \tau_D = 1$ , we obtain ADOS plots (Fig. 6). From the spectra, we find that localized states for up and down spin electrons appear at two distinct energies. When the Fermi energy is set to either of these values, one spin species is completely blocked while the other passes freely, resulting in full spin polarization. A similar behavior can also be observed at other energies.

Here it is important to note that the arrangement of local magnetic moments at different lattice sites within each diamond plaquette plays a crucial role. If we assume that in alternating plaquettes, all moments are aligned along the  $+Z$  direction, while in the other plaquettes they are aligned along the  $-Z$  direction to maintain zero net magnetization, no mismatch between the up and down spin channels occurs. Similarly, for many other possible configurations, the up and down spin DOS remain identical, preventing any spin filtration.

## B. Spin-Selective Transmission, Filtration, and Related Issues

Following the above analysis of spectral behavior, in this sub-section we focus on spin-selective transmission probabilities, spin currents, the degree of spin filtration, and related aspects.

Let us begin with Fig. 7, which presents the spin-dependent transmission probabilities, currents and spin polarization for an AFM diamond network with  $N = 10$ . Figure 7(a) shows the variation in up and down spin transmission probabilities, clearly revealing their mismatch. Over a wide energy region, electrons of one spin propagate, while those of the other spin are completely blocked. In the transmitting zone, multiple resonant peaks are observed, all of which are directly associated with the available energy channels of the conductor. The widths of these peaks are determined by the coupling strength between the conductor and the side-attached leads. Under weak coupling, the peaks are sharp, whereas they broaden with increasing coupling strength—an effect well known in the literature. Figures 7(b) and (c) present the spin-dependent currents and the corresponding spin polarizations for two distinct Fermi energies:  $E_F = -1$  and  $E_F = 1$ , respectively. When  $E_F = -1$ ,

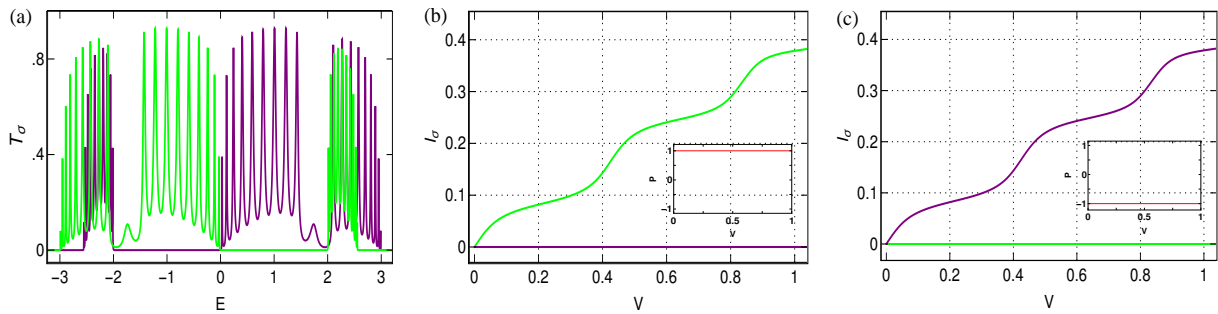


FIG. 7: (Color online). (a) Transmission-energy spectrum of two spin channels for the system with number of plaquettes  $N = 10$ . A finite mismatch between the two spin bands is clearly observed, resulting in different energy zones where one spin is completely blocked while the other is transmitted. The spin-dependent currents at  $\mathcal{T} = 10K$  for two different Fermi energies,  $E_F = -1$  and  $E_F = 1$ , are shown in (b) and (c), and, the insets shows the polarization curve with bias voltage at these Fermi energies respectively. The green curve represents the up spin, while the purple curve represents the down spin in (a)–(c).

only the up-spin current is observed within the chosen bias window, while the down-spin current is completely suppressed, reflecting the nature of the transmission profiles. As a result, 100% spin polarization is achieved, as shown in the inset of Fig. 7(b). The step-like behavior of the current arises from the sharpness of the resonant transmission peaks. An exactly opposite scenario occurs when the Fermi energy is shifted to  $E_F = 1$ : only the down-spin current is present, leading to  $-100\%$  spin polarization (Fig. 7(c) and its inset), in agreement with the transmission curves. Thus, by selectively tuning the Fermi energy, complete spin polarization can be achieved and sustained over a large bias window.

Next, we examine the angular dependence of spin transmission. The polar angle for site A is denoted as  $\theta$ , while for site B, it is  $\pi + \theta$ . This configuration ensures an antiferromagnetic arrangement in each plaquette. We analyze the effect of magnetic moment rotation

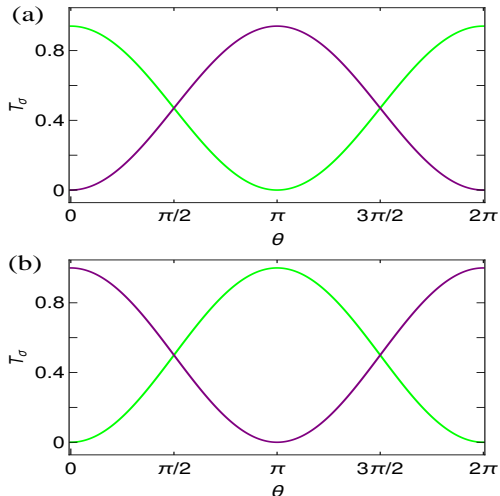


FIG. 8: (Color online). Transmission probabilities as a function of the polar angle. The magnetic moment at site A is oriented at an angle  $\theta$ , while at site B, it is  $\pi + \theta$ . The Fermi energy is set at  $E_F = -1$  in (a) and at  $E_F = 1$  in (b). The color convention follows that of Fig. 7, where the green curve represents up-spin and the purple curve represents down-spin.

on spin filtration by calculating the transmission prob-

ability, spin-dependent current, and polarization. Figures 8(a) and (b) show the transmission probabilities  $T_\uparrow$  (green) and  $T_\downarrow$  (purple) for two different Fermi energies,  $E_F = -1$  and  $E_F = 1$ . These curves exhibit sinusoidal variations, with the maximum phase difference occurring when the polar angle is an integer multiple of  $\pi$ . The same pattern is observed in the spin-dependent currents shown in Figs. 9(a) and (c). Thus, polarization reaches

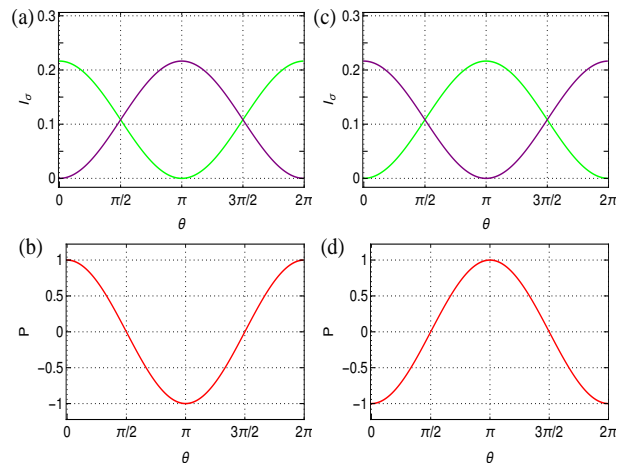


FIG. 9: (Color online). Spin-dependent currents and spin polarization as a function of the rotation angle of the magnetic moment. The green and purple curves in the first row represent up and down spin currents, respectively, while the red curve in the second row represents spin polarization. The Fermi energy is set at  $E_F = -1$  for (a) and (b), and at  $E_F = 1$  for (c) and (d). Other parameters are the same as in Fig. 8.

its maximum when the polar angle is  $\theta = n\pi$ . Notably, polarization can be switched from 1 to -1 by adjusting the polar angle from  $2n\pi$  to  $(2n + 1)\pi$ .

So far, we have discussed spin separation in the antiferromagnetic system in the context of localization. The energy gap between conducting and localized states plays a crucial role in achieving large polarization. The localized level is  $N$ -fold degenerate for both spin orientations, but this degeneracy is lifted in the presence of a magnetic flux ( $\phi$ ). We previously examined the effect of magnetic flux in the nonmagnetic case; now, we focus on its impact

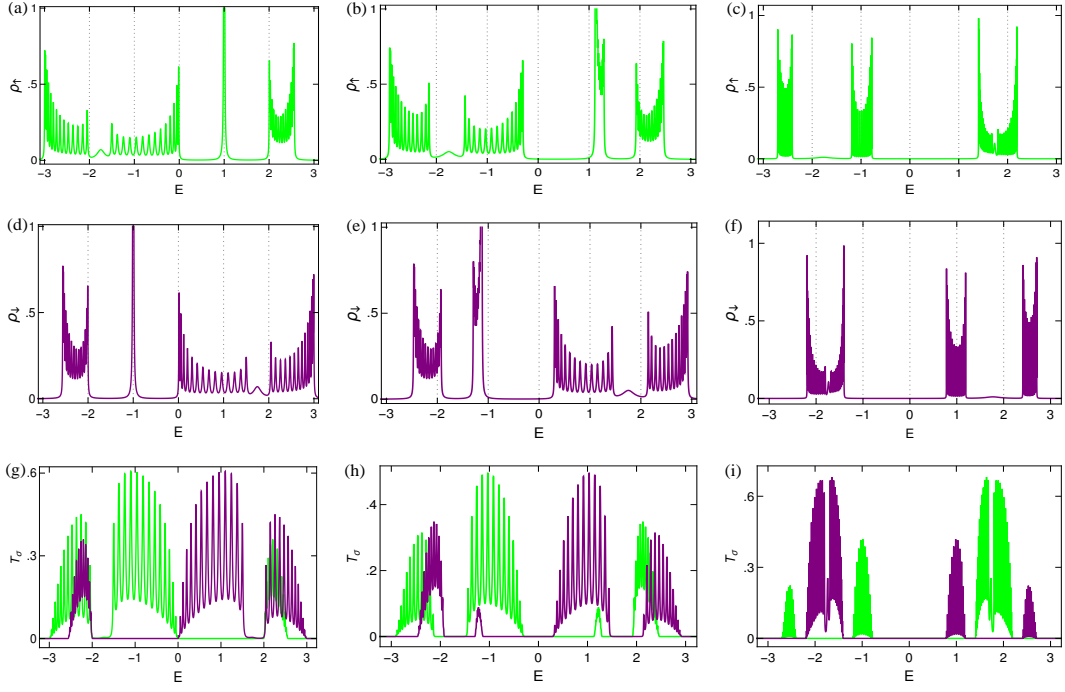


FIG. 10: (Color online). Density of states (DOS) and transmission probabilities at different values of magnetic flux  $\phi$ . Here, the spin-dependent scattering factor  $h = 1$ , and the number of diamond plaquettes is  $N = 15$ . The green and purple curves correspond to up-spin and down-spin electrons, respectively. The first column represents  $\phi = 0$ , the second column  $\phi = 0.2\phi_0$ , and the third column  $\phi = 0.4\phi_0$ . Panels (a-c) show the DOS for up-spin electrons, (d-f) for down-spin electrons, and (g-i) the transmission probabilities for both spins.

on the antiferromagnetic system.

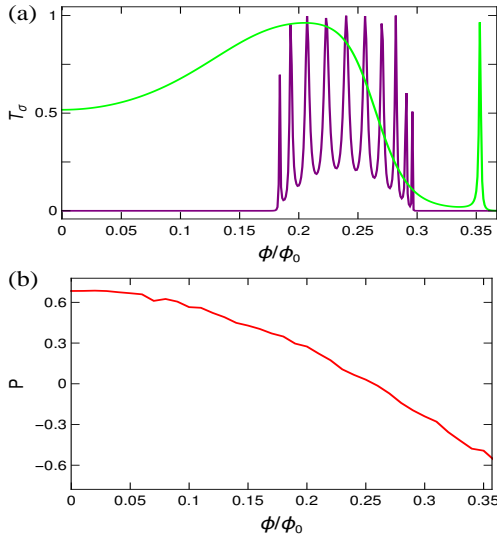


FIG. 11: (Color online). A clearer visualization of the specific role of magnetic flux  $\phi$ . (a) Transmission probability as a function of flux, where the green curve represents up-spin and the purple curve denotes down-spin. (b) Spin polarization regulation at  $\mathcal{T} = 50$  K and voltage  $V = 2$  V. The magnetic moment arrangement remains unchanged:  $\theta = \pi$  for A-type sites and  $\theta = 0$  for B-type sites. Here we set  $E_F = -1.25$ .

In the absence of  $\phi$ , a localized energy level appears at  $E = 1$  for up-spin electrons, along with three conducting sub-bands at different energy levels, separated

by a significant energy gap (see Fig. 10). When  $\phi$  is in-

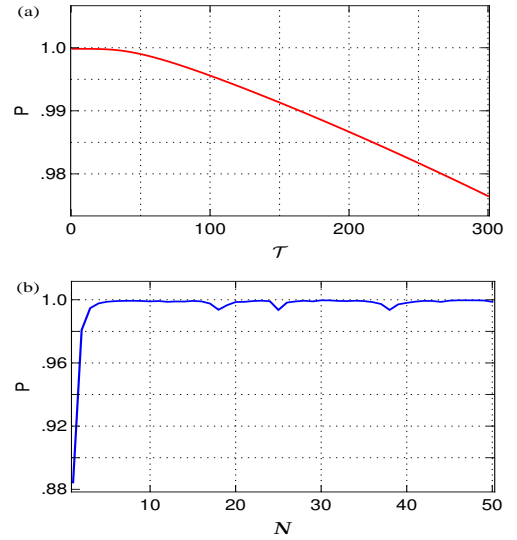


FIG. 12: (Color online). Effects of temperature and system size on spin polarization. (a) Polarization versus temperature for  $N = 10$  plaquettes, with  $E_F = -1$  and  $V = 2$  V. (b) Polarization versus system size at  $\mathcal{T} = 50$  K. Other parameters remain the same as in Fig. 7.

roduced, the localized level disappears, and conducting bands emerge in this regime. The energy gap is also affected by the presence of magnetic flux. As  $\phi$  increases, the newly formed conduction band widens and eventually merges with the nearest conduction band. Similar

behavior is observed for down-spin electrons, where delocalization occurs at  $E = -1$  and overlaps with the up-spin energy band. Reflecting the up and down spin DOS spectra, transmission probabilities are obtained for the resonant energy channels (last row of Fig. 10). At  $\phi = 0.5\phi_0$ , transmission in both spin channels is suppressed due to complete localization (not shown here in Fig. 10), similar to the nonmagnetic case. Beyond this, periodicity restores the system at  $\phi = 1$ .

Figure 11 plots the transmission probability and polarization as a function of  $\phi$ , with the Fermi energy set at  $E_F = -1.25$ . In the absence of  $\phi$ , up-spin electrons dominate. As  $\phi$  increases to approximately  $0.18\phi_0$ , down-spin transmission begins, eventually surpassing up-spin transmission. This transition is also reflected in the polarization curve, where an initially positive polarization reverses with increasing flux. Thus, the polarity of spin polarization can be tuned simply by adjusting the magnetic flux at a fixed Fermi energy.

All spin currents and polarization values were evaluated at nonzero temperature. Notably, polarization remains stable even at room temperature (300 K), as the energy gap between conducting and localized states is significantly larger than thermal energy ( $k_B\mathcal{T}$ ). As shown in Fig. 12(a), spin polarization varies by only 2% over the temperature range 0 – 300 K, indicating robust polarization at room temperature. Additionally, polarization remains nearly constant for  $N > 5$ , suggesting efficient spin filtration across a broad range of system sizes.

### C. Semiconductor Properties

In this sub-section, we discuss how different spin channels can exhibit distinct semiconductor properties by tuning the spin-dependent scattering  $h$ . According to renormalization theory, in the absence of a magnetic flux, a degenerate localized level (LL) appears at  $E = \epsilon_A$ . The on-site energy for up and down spins is given by  $\epsilon + h$  and  $\epsilon - h$ , respectively, as shown in Fig. 1.

When  $h = 0$ , the LL for both spin channels is located at  $E = 0$  (assuming  $\epsilon = 0$ ), meaning there is no band separation between up-spin and down-spin electrons. The energy gap between the conduction band and the LL depends on the on-site potential energy difference between A-type and B-type atoms. In our configuration, the energy difference for up-spin electrons is  $\epsilon_A - \epsilon_B = +2h$ , while for down-spin electrons, it is  $\epsilon_A - \epsilon_B = -2h$ . Consequently, at  $h = 0$ , there is no energy gap, allowing electrons to transmit freely even where LL is located.

In the previous section, we discussed the case of  $h = 1$ , where a high degree of spin polarization can be achieved. The LL for each spin channel is positioned to open a large energy gap (approximately 1 eV) between the conduction band and the LL. Specifically, the LL for up-spin electrons is located at  $E = h$ , while for down-spin electrons, it is at  $E = -h$ .

An interesting scenario arises when the position of the localized level and the energy gap can be selectively tuned. For  $h < 0.5$ , the LL resides within one of the conduction bands for both spin channels, as shown in

Figs. 13(a) and (d). In this case, the LL becomes insignificant as electrons can transmit through the neighboring conduction band by gaining thermal energy ( $k_B\mathcal{T}$ , approximately 0.025 eV at room temperature).

For  $h = 0.5$ , the LL (see Figs. 13(b) and (e)) is located at the boundary of the conduction band. As  $h$  increases further, the LL moves out of the conduction band, cre-

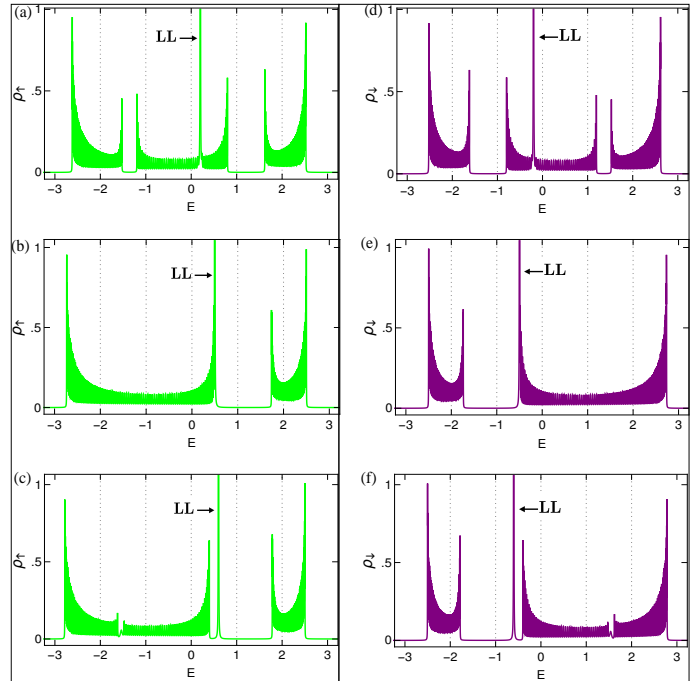


FIG. 13: (Color online). Tuning of the localized level by varying the strength of spin-dependent scattering factor  $h$ . The ADOS for up-spin (green) and down-spin (purple) electrons is shown for three values of  $h$ : (a, d)  $h = 0.2$ , (b, e)  $h = 0.5$ , and (c, f)  $h = 0.6$ . The diamond chain consists of  $N = 50$  plaquettes.

ating an energy gap. At  $h = 0.6$ , as shown in Fig. 13(c), the energy gap between the conduction band and the LL is asymmetric, with a smaller gap on the left side compared to the right. If electrons in the left-side band are excited, they transition to the LL. However, once they reach the LL, they become localized. This results in the formation of holes in the left-side band, which are up-spin polarized.

Similarly, in Fig. 13(f), the LL for down-spin electrons appears at  $E = -0.6$ , opening a larger gap on the left side. A small perturbation can compensate for the energy gap on the right side, allowing electrons in the LL to transition to the conduction band with minimal energy input. This results in an  $n$ -type semiconductor with down-spin-polarized electrons. Thus, by tuning the spin-dependent scattering strength and appropriately positioning the Fermi energy, both  $p$ -type and  $n$ -type semiconductors can be realized in different spin channels.

If an  $n$ -type semiconductor with up-spin-polarized electrons is desired, a slight modification in the arrangement of magnetic atoms in the diamond plaquette is required. By reversing the magnetic moment direction in A-type and B-type atoms—setting the A-type atom's

moment along the  $+z$ -axis and the B-type atom's moment along the  $-z$ -axis—the spin bands are inverted in energy. In this configuration, the LL for up-spin electrons shifts to  $E = -h$ , while for down-spin electrons, it moves to  $E = h$ . Consequently, selecting  $h = 0.6$  would produce down-spin-polarized holes and an excess of up-spin-polarized electrons. Therefore, both types of semiconductors can be engineered with either up-spin or down-spin polarization by appropriately configuring the system.

#### IV. CLOSING REMARKS

In this work, we introduce an antiferromagnetic model that fulfills two key functions: (i) generating and regulating spin polarization and (ii) exhibiting semiconducting behavior, where the spin state of the majority carriers can be controlled. The formation of localized levels plays a crucial role in this mechanism. Our model is free from disorder and external electric fields. By simulating the quantum system within a tight-binding framework, we characterize its transport properties using Green's function formalism. All the required energy dispersion relations are derived analytically.

A distinctive feature of the energy spectrum is the trio combination of conduction, gap, and localization bands. In low-dimensional systems, localized states typically arise from either random or correlated disorder. In the former, Anderson localization<sup>36</sup> occurs for any finite disorder, whereas in correlated disorder systems—such as the Aubry-André-Harper model<sup>37–39</sup>—localization emerges beyond a critical disorder threshold. In contrast, our model exhibits a sharply localized, highly degenerate energy level alongside conducting energy channels solely due to the network's geometry. This unique property allows complete blocking of one spin channel while permitting transmission through the other, distinguishing our model within the field.

To ensure a comprehensive understanding, we provide detailed theoretical explanations, making this work self-contained. Additionally, various fabrication techniques could facilitate the realization of this diamond plaquette array, including lithographic methods<sup>41</sup>, molecular beam epitaxy<sup>42</sup>, and droplet epitaxy<sup>43</sup>. The magnetic moment arrangement can be controlled via doping with magnetic nanoparticles<sup>44</sup>.

We believe our findings contribute to the advancement of efficient spin-filter devices in small-scale systems and provide a valuable example for the expanding field of antiferromagnetic spintronics.

#### Appendix A: Energy dispersion relations

We take the nonmagnetic case and numerically solve the E-k relation for three cases. Here the parameters are

specified as  $\epsilon_A = \epsilon_B = 0$  and  $t = t' = 1$ .

#### ■ Solution of dispersion relation for general $\phi$

The four dispersive energy levels correspond to Eq. 12 are given by

$$E_1 = -E_2 = \frac{1}{2}(\alpha + \beta) \quad (\text{A1a})$$

$$E_3 = -E_4 = \frac{1}{2}(\alpha - \beta) \quad (\text{A1b})$$

where

$$\alpha = \left[ \frac{1}{q} (20.57 - 10.07 \cos 4\eta) + 0.26q + 3.33 \right]^{1/2}$$

and

$$\beta = \left[ 10 - \alpha^2 - \frac{8}{\alpha} \cos 2\eta \cos k \right]^{1/2}.$$

The factor  $q$  is expressed as

$$q = \left[ 470 - 720 \cos 4\eta + 432 \cos^2 2\eta \cos^2 k + \left\{ 55296 (\cos 4\eta - 2.04)^3 + 518400 (0.65 - \cos 4\eta + 0.6 \cos^2 2\eta \cos^2 k)^2 \right\}^{1/2} \right]^{1/3}.$$

#### ■ Solution of dispersion relation for $\phi = 0$

Here we get one localized level and three dispersive levels as

$$E_1 = 0 \quad (\text{A2a})$$

$$E_2 = 3.46q_0^{-3} + 0.48q_0 \quad (\text{A2b})$$

$$E_3 = -\frac{1}{q_0} (1.73 - 7j) - q_0 (0.24 + 0.42j) \quad (\text{A2c})$$

$$E_4 = -\frac{1}{q_0} (1.73 + 7j) - q_0 (0.24 - 0.42j). \quad (\text{A2d})$$

#### ■ Solution of dispersion relation for $\phi = 0.5\phi_0$

Here we get four localized energy levels as

$$E_1 = -E_2 = 1 \quad (\text{A3a})$$

$$E_3 = -E_4 = 2. \quad (\text{A3b})$$

\* Electronic address: [debjanidasgupta34@gmail.com](mailto:debjanidasgupta34@gmail.com)

† Electronic address: [santanu.maiti@isical.ac.in](mailto:santanu.maiti@isical.ac.in)

- <sup>1</sup> Y. Xu, S. Wang, and K. Xia, Phys. Rev. Lett. **100**, 226602 (2008).
- <sup>2</sup> Xiao Hu, Adv. Mater. **24**, 294 (2012).
- <sup>3</sup> T. Jungwirth, X. Marti, P. Wadley, and J. Wunderlich, Nat. Nanotechnol. **11**, 231 (2016).
- <sup>4</sup> V. Baltz, A. Manchon, M. Tsoi, T. Moriyama, T. Ono, and Y. Tserkovnyak, Rev. Mod. Phys. **90**, 015005 (2018).
- <sup>5</sup> T. Jungwirth, J. Sinova, X. Matri, J. Wunderlich, and C. Felser, Nat. Phys. **14**, 200 (2018).
- <sup>6</sup> M. B. Jungfleisch, W. Zhang, and A. Hoffmann, Phys. Lett. A **13**, 382 (2018).
- <sup>7</sup> R. A. Duine, K. Lee, S. P. Parkin, and M. D. Stiles, Nat. Phys. **14**, 217 (2018).
- <sup>8</sup> P. Némec, M. Fiebig, T. Kampfath, and A. V. Kimel Nat. Phys. **14**, 229 (2018).
- <sup>9</sup> G. A. Prinz, Phys. Today **48**, 58 (1995).
- <sup>10</sup> G. A. Prinz, Science **282**, 1660 (1998).
- <sup>11</sup> S. A. Wolf, D. D. Awschalom, R. A. Buhrman, J. M. Daughton, S. von Molnár, M. L. Roukes, A. Y. Chtchelkanova, and D. M. Treger, Science **294**, 1488 (2001).
- <sup>12</sup> I. Žutić, J. Fabian, and S. Das Sarma, Rev. Mod. Phys. **76**, 323 (2004).
- <sup>13</sup> J. Fabian, A. M. Abiague, C. Ertler, P. Stano, and I. Žutić, Acta Phys. Slovaca **57**, 565 (2007).
- <sup>14</sup> R. Jansen, S P Dash, S Sharma, and B C Min, Semicond. Sci. Technol. **27**, 083001 (2012).
- <sup>15</sup> C. Marrows, Science **351**, 558 (2016).
- <sup>16</sup> P. Wadely *et al.*, Science **351**, 587 (2016).
- <sup>17</sup> S. Jenkins, A. Meo, L. Elliott, S. Piotrowski, M. Bapna, R. Chantrell, S. Majetich and R. Evans, J. Phys. D: Appl. Phys. **53**, 044001(2020).
- <sup>18</sup> K. Garello, C. O. Avci, I. M. Miron, M. Baumgartner, A. Ghosh, S. Auffret, O. Boulle, G. Gaudin, and P. Gambardella, Appl. Phys. Lett. **105**, 212402 (2014).
- <sup>19</sup> A. Machon, H. -C. Koo, J. Nitta, S. M. Frolov, and R. A. Duine, Nat. Mater. **14**, 871 (2015).
- <sup>20</sup> M. Dey, S. K. Maiti, S. Sil, and S. N. Karmakar, J. Appl. Phys. **114**, 164318 (2013).
- <sup>21</sup> Y. A. Bychkov and E. I. Rashba, J. Phys. C: Solid State Phys. **17**, 6039 (1984).
- <sup>22</sup> G. Dresselhaus, Phys. Rev. **100**, 580 (1955).
- <sup>23</sup> Y.-H. Su, S.-H. Chen, C. D. Hu, and C.-R. Chang, J. Phys. D: Appl. Phys. **49**, 015305 (2015).
- <sup>24</sup> D. Das Gupta and S. K. Maiti, J. Phys.: Condens. Matter **32**, 505803 (2020).
- <sup>25</sup> D. Das Gupta and S. K. Maiti, Phys. Rev. B **106**, 125420 (2022).
- <sup>26</sup> D. Das Gupta, S. K. Maiti, L. M. Pérez, J. H. O. Silva, and D. Laroze, Results Phys. **52**, 106918 (2023).
- <sup>27</sup> D. Bercioux, M. Governale, V. Cataudella, and V. M. Ramaglia, Phys. Rev. Lett. **93**, 056802 (2004).
- <sup>28</sup> A. Aharony, O. Entin-Wohlman, Y. Tokura, and S. Katsumoto, Phys. Rev. B **78**, 125328 (2008).
- <sup>29</sup> S. Sil, S. K. Maiti, and A. Chakrabarti, Phys. Rev. B **79**, 193309 (2009).
- <sup>30</sup> B. Pal and A. Chakrabarti, Phys. Rev. B **85**, 214203 (2012).
- <sup>31</sup> M. Saha and S. K. Maiti, Phys. Lett. A **380**, 1450 (2016).
- <sup>32</sup> M. Patra, S. K. Maiti, and S. Sil, J. Phys.: Condens. Matter **31**, 355303 (2019).
- <sup>33</sup> S. Sarkar and S. K. Maiti, Phys. Rev. B **100**, 205402 (2019).
- <sup>34</sup> S. Datta, *Quantum transport in mesoscopic system*, Cambridge University Press, Cambridge (1995).
- <sup>35</sup> Y. Gefen, Y. Imry, and M. Ya. Azbel, Phys. Rev. Lett. **52**, 129 (1984).
- <sup>36</sup> P. W. Anderson, Phys. Rev. **109**, 1492 (1958).
- <sup>37</sup> S. Aubry and G. Andre, in *Group Theoretical Methods in Physics*, edited by L. Horwitz and Y. Ne'eman, Annals of the Israel Physical Society Vol. 3 (American Institute of Physics, New York, 1980), p. 133.
- <sup>38</sup> B. Sokoloff, Phys. Rep. **126**, 189 (1985).
- <sup>39</sup> S. Sil, S. K. Maiti, and A. Chakrabarti, Phys. Rev. Lett. **101**, 076803 (2008).
- <sup>40</sup> M. Sarkar, M. Dey, S. K. Maiti, and S. Sil, Phys. Rev. B **102**, 195435 (2020).
- <sup>41</sup> S. M. Weekes, F. Y. Ogrin, and W. A. Murray, Langmuir **20**, 11208 (2004).
- <sup>42</sup> B. Fuhrmann, H. S. Leipner, and H. -R. Höche, Nano. Lett. **5**, 2524 (2005).
- <sup>43</sup> D. Xia, Z. Ku, S. C. Lee, and S. R. J. Brueck, Adv. Mater. **23**, 147 (2010).
- <sup>44</sup> P. Guardia, A. Labarta, and X. Batlle, J. Phys. Chem. C **115**, 390 (2011).